

An ultrasonic multi-wave focusing and imaging method for linear phased arrays

Yu-Xiang Dai(戴宇翔), Shou-Guo Yan(阎守国), and Bi-Xing Zhang(张碧星)

Citation: Chin. Phys. B, 2021, 30 (**7**): 074301. DOI: 10.1088/1674-1056/abf91d
Journal homepage: http://cpb.iphy.ac.cn; http://iopscience.iop.org/cpb

What follows is a list of articles you may be interested in

Ultrasonic beam focusing characteristics of shear-vertical waves for contact-type linear phased array in solid

Yu-Xiang Dai(戴宇翔), Shou-Guo Yan(阎守国), Bi-Xing Zhang(张碧星)
Chin. Phys. B, 2020, 29 (**3**): 034304. DOI: 10.1088/1674-1056/ab69ed

Simulation of acoustic fields emitted by ultrasonic phased array in austenitic steel weld

Zhong-Cun Guo(郭忠存), Shou-Guo Yan(阎守国), Bi-Xing Zhang(张碧星)
Chin. Phys. B, 2019, 28 (**11**): 114302. DOI: 10.1088/1674-1056/ab4d41

Lamb waves topological imaging combining with Green's function retrieval theory to detect near filed defects in isotropic plates

Hui Zhang(张辉), Hai-Yan Zhang(张海燕), Meng-Yun Xu(徐梦云), Guo-Peng Fan(范国鹏), Wen-Fa Zhu(朱文发), Xiao-Dong Chai(柴晓冬)
Chin. Phys. B, 2019, 28 (**7**): 074301. DOI: 10.1088/1674-1056/28/7/074301

Influence exerted by bone-containing target body on thermoacoustic imaging with current injection

Yan-Hong Li(李艳红), Guo-Qiang Liu(刘国强), Jia-Xiang Song(宋佳祥), Hui Xia(夏慧)
Chin. Phys. B, 2019, 28 (**4**): 044302. DOI: 10.1088/1674-1056/28/4/044302

An acoustic Maxwell's fish-eye lens based on gradient-index metamaterials

Bao-guo Yuan(袁保国), Ye Tian(田野), Ying Cheng(程营), Xiao-jun Liu(刘晓峻)
Chin. Phys. B, 2016, 25 (**10**): 104301. DOI: 10.1088/1674-1056/25/10/104301

An ultrasonic multi-wave focusing and imaging method for linear phased arrays*

Yu-Xiang Dai(戴宇翔)[1,2], Shou-Guo Yan(阎守国)[1,†], and Bi-Xing Zhang(张碧星)[1,2]

[1] *Key Laboratory of Acoustics, Institute of Acoustics, Chinese Academy of Sciences, Beijing* 100190, *China*
[2] *University of Chinese Academy of Sciences, Beijing* 100190, *China*

(Received 5 March 2021; revised manuscript received 27 March 2021; accepted manuscript online 19 April 2021)

To overcome the inherent limits of traditional single wave imaging for nondestructive testing, the multi-wave focusing and imaging method is thoroughly studied. This method makes the compressional waves and shear waves focused in both emission and reception processes, which strengthens the focusing energy and improves the signal-to-noise ratio of received signals. A numerical model is developed to study the characteristics of a multi-wave focusing field. It is shown that the element width approaching 0.8 wavelengths of shear waves can keep a balance between the radiation energy of two waves, which can achieve a desirable multi-wave focusing performance. And an experiment using different imaging methods for a linear phased array is performed. It can be concluded that due to the combination of the propagation and reflection characteristics of two waves, the multi-wave focusing and imaging method can significantly improve the imaging distinguishability of defects and expand the available sweeping range to a sector of $-65°$ to $65°$.

Keywords: multi-wave focusing, ultrasonic imaging, phased array, non-destructive testing

PACS: 43.20.+g, 43.35.+d, 43.38.+n **DOI:** 10.1088/1674-1056/abf91d

1. Introduction

Nowadays, ultrasonic imaging with phased arrays is an important technology and is widely applied in various fields, including non-destructive testing (NDT),[1–4] sonar,[5,6] medical diagnosis[7–9] and so on. With rapid development of the technology, the industry makes higher requirements for imaging resolution in NDT.

Solid materials support the propagation of multiple waves,[10] especially the compressional wave (P-wave) and shear wave (S-wave), each of which carries a specific type of imaging information.[11] However, only a single type of wave is employed by the traditional ultrasonic imaging technology in the field of NDT. Conventionally, phased arrays mostly utilize P-waves to form ultrasonic images due to the convenience of excitation. And the S-waves are typically employed to perform inspections for components with complex structures, where the P-waves cannot play an effective role.[12–14] Actually, the S-wave is much more sensitive to the shear modules than the P-wave, which indicates that it can provide additional information for imaging.[15–17] Furthermore, the shorter wavelength of the S-wave can provide higher imaging resolution. Based on these properties, Ye *et al.*[15] employed shear-wave imaging to reveal the mechanical characterization of bones, which is helpful for the diagnosis of osteoporosis. However, the ultrasonic imaging method using a single wave cannot provide comprehensive information of the medium, which makes it difficult to further improve the imaging quality.

A popular approach used to improve the imaging resolution is to combine multiple types of imaging methods, such as acousto-optical tomography, which has achieved considerable development in medical research.[11,18] For example, Emelianov *et al.*[18] achieved super-resolution imaging by combining ultrasonic and photoacoustic imaging. However, the high cost limits its application in NDT. On the other hand, Zhang *et al.*[19] proposed the multi-mode total focusing method for phased arrays to improve the imaging resolution, which uses several propagation modes. However, this method is based on the total focusing method (TFM), so it suffers from a limitation of long computation time in the post-processing of tremendous data,[20] which makes it hard to implement real-time imaging. Besides, the TFM only employs a single element in emission, which greatly degrades the energy of acoustic waves. However, combination imaging using several propagation modes of waves can form some artifacts in images, which results in misinterpretation.[21]

Zhang *et al.*[22] proposed an ultrasonic multi-wave focusing and scanning method applied in NDT, which uses multiple waves to provide more comprehensive information. Its principle is to simultaneously focus the compressional wave and shear wave propagating in a solid medium at the focal point. In this method, the multiple waves excited by all the elements are focused to greatly strengthen the energy of the scanning beam, which improves the signal-to-noise ratio of received signals and thus avoids the formation of artifacts in images. More importantly, this method can implement real-time imaging, which is of great importance in practical appli-

*Project supported by the National Natural Science Foundation of China (Grant No. 11774377).
†Corresponding author. E-mail: yanshouguo@mail.ioa.ac.cn
© 2021 Chinese Physical Society and IOP Publishing Ltd

cation. In previous work of Zhang *et al.*,[22] only the focusing emission process was discussed. And in this paper, a more in-depth study is performed. Firstly, the influence of array parameters on multi-wave focusing performance is discussed to optimize the phased arrays, which is the fundamental requirement to achieve a desirable multi-wave focusing performance for linear phased arrays. Secondly, the implementation process is introduced in detail, including the focusing emission process for scanning and the focusing reception process for imaging, where the double pulse method and multi-wave imaging method are respectively proposed to implement them. Lastly, the multi-wave beam focusing and imaging characteristics are thoroughly studied, and reveal the essential reason why the multiwave focusing method can improve the signal-to-noise ratio of echoes.

In addition, it should be noted that the traditional arrays have to be coupled with a wedge to generate S-waves from mode conversion,[23,24] which is hard to employ to realize multi-wave focusing in the emission process. But our recent study has proved the feasibility of employing contact-type linear phased arrays for shear-wave focusing imaging.[23] Based on this work, multi-wave focusing can be successfully realized using the contact-type linear phased arrays.

The remainder of the present paper is organized as follows. Section 2 introduces the specific implementation of the multi-wave focusing process in detail, where the multi-wave focusing reception method for imaging is proposed. Section 3 studies the multi-wave focusing performance and obtains the optimal design parameters of the linear phased arrays. Section 4 performs the imaging experiment of different focusing methods to verify the numerical results. Finally, Section 5 summarizes the work.

2. Implementation of multi-wave focusing process

The implementation of multi-wave focusing technology consists of two processes, which are the focusing emission process for scanning and the focusing reception process for imaging, respectively. In this section, the two above processes are introduced in detail. And the theoretical formulas of a multi-wave focusing field excited by linear phased arrays are also given. Moreover, the reflection characteristics of P- and S-waves are analyzed to reveal the advantages of multi-wave focusing technology in imaging.

2.1. Radiation acoustic field

As shown in Fig. 1, a linear phased array of N elements is assumed to be placed on the free surface of an elastic solid that is regarded as a two-dimensional half-space. The element width is $2a$, and the inter-element spacing is d. Here, the Cartesian coordinate system and polar coordinate system are both introduced for convenience. And the origin of the coordinate system coincides with the geometric center of the array. The elements are numbered sequentially along the positive x direction. Note that the S-wave refers to a shear vertical wave (SV-wave), and the shear horizontal wave (SH-wave) is not taken into consideration for simplification.

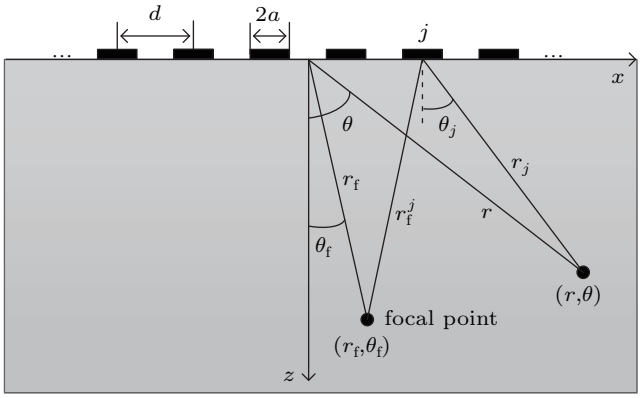


Fig. 1. A model illustration of the transducer array for multi-wave focusing, where (r_f, θ_f) is the focal point, r_f is the focal length and θ_f is the steering angle.

As shown in Fig. 1, r_j and θ_j are the propagation distance and azimuth angle from the j-th element to the arbitrary point (r, θ) in the field, which satisfies the following geometric relationship:

$$\begin{aligned} r_j &= \sqrt{(r\cos\theta)^2+\left(r\sin\theta-\frac{2j-N-1}{2}d\right)^2}, \\ \theta_j &= \arctan\frac{r\sin\theta-\dfrac{2j-N-1}{2}d}{r\cos\theta}. \end{aligned} \tag{1}$$

And the propagation distance from the j-th element to the focal point is denoted as r_f^j, which satisfies the following relationship:

$$r_\mathrm{f}^j=\sqrt{(r_\mathrm{f}\cos\theta_\mathrm{f})^2+\left(r_\mathrm{f}\sin\theta_\mathrm{f}-\frac{2j-N-1}{2}d\right)^2}. \tag{2}$$

The theoretical formulas of the field excited by a single element can be obtained from our previous study,[23] which can be expanded into the following form:

$$\begin{aligned} u_x(x,z,t) &= \frac{1}{2\pi}\int_{-\infty}^{+\infty}F(\omega)\int_{-\infty}^{+\infty}\frac{2\sin(ka)}{\mu kG(k)}\cdot\Big\{\mathrm{i}k\left(k_\mathrm{s}^2-2k^2\right) \\ &\quad\times\exp\left[\mathrm{i}\left(kx+\alpha z-\omega t\right)\right]-2\mathrm{i}k\alpha\beta \\ &\quad\times\exp\left[\mathrm{i}\left(kx+\beta z-\omega t\right)\right]\Big\}\mathrm{d}k\,\mathrm{d}\omega, \\ u_z(x,z,t) &= \frac{1}{2\pi}\int_{-\infty}^{+\infty}F(\omega)\int_{-\infty}^{+\infty}\frac{2\sin(ka)}{\mu kG(k)}\cdot\Big\{\mathrm{i}\alpha\left(k_\mathrm{s}^2-2k^2\right) \\ &\quad\times\exp\left[\mathrm{i}\left(kx+\alpha z-\omega t\right)\right]+2\mathrm{i}k^2\alpha \\ &\quad\times\exp\left[\mathrm{i}\left(kx+\beta z-\omega t\right)\right]\Big\}\mathrm{d}k\,\mathrm{d}\omega, \end{aligned} \tag{3}$$

where u_x and u_z are the displacements in the x- and z-direction, ω is the angular frequency, k is the wave number in the x-direction, μ is Lame's constant, $k_\mathrm{s}=\omega/c_\mathrm{s}$, $k_\mathrm{p}=\omega/c_\mathrm{p}$, c_p

and c_s are the velocities of P- and S-waves, $\alpha = (k_p^2 - k^2)^{1/2}$, $\beta = (k_s^2 - k^2)^{1/2}$, $G(k) = 4k^2\alpha\beta + (k_s^2 - 2k^2)^2$ and $F(\omega)$ is the frequency domain form of the force function exciting the elements.

If the position is located in the polar coordinate, the displacements in the x- and z-direction can be rewritten with the following relationships:

$$u_x(r,\theta,t) = u_x(x,z,t)\big|_{x=r\sin\theta, z=r\cos\theta},$$
$$u_z(r,\theta,t) = u_z(x,z,t)\big|_{x=r\sin\theta, z=r\cos\theta}. \quad (4)$$

2.2. Focusing in emission

The double pulse method is employed to implement the multi-wave focusing emission process, where each element is sequentially excited by two transient pulses. It should be noted that each pulse can excite each element to generate both P-waves and S-waves. And due to the difference in wave speeds, the S-waves generated by the first pulse and the P-waves generated by the second pulse can be simultaneously focused at the focal point by controlling the time delays on the elements. Specifically, the following steps are taken:

(i) The position of the focal point (r_f, θ_f) is predetermined, then r_f^j can be calculated with Eq. (2).

(ii) Each element is excited by the first pulse to generate the P- and S-waves. To make all the S-waves focus at the focal point, the first pulse on each element should be delayed respectively. The time delay is determined by the propagation distance r_j, so it is necessary to select an element as a reference. Here, by taking the 1st element as the reference element, then the time delay required for the first pulse on the j-th element can be given as follows:

$$\tau_j = \frac{r_1 - r_j}{c_s}. \quad (5)$$

(iii) Similarly, the P-waves excited by the second pulse on each element are also requested to be simultaneously focused at the focal point with the S-waves generated by the first pulse. And the time delay required for the second pulse on the j-th element is given as follows:

$$\delta_j = \tau_j + \frac{r_j}{c_s} - \frac{r_j}{c_p}. \quad (6)$$

Then, the multi-wave focusing field can be regarded as the synthesis of the fields contributed by all elements

$$u_x^f(r,\theta,t) = \sum_{j=1}^{N}[u_x(r_j,\theta_j,t-\tau_j) + u_x(r_j,\theta_j,t-\delta_j)],$$
$$u_z^f(r,\theta,t) = \sum_{j=1}^{N}[u_z(r_j,\theta_j,t-\tau_j) + u_z(r_j,\theta_j,t-\delta_j)]. \quad (7)$$

The total displacements of any arbitrary position in the field can be written as

$$U(r,\theta,t) = \sqrt{[u_x^f(r,\theta,t)]^2 + [u_z^f(r,\theta,t)]^2}. \quad (8)$$

To analyze the multi-wave focusing performance, the directivity function can be defined as[14]

$$H(\theta) = \frac{\max[U(r_f,\theta,t)]}{\max[U(r_f,\theta_f,t)]}, \quad (9)$$

where max[ ] is an operator that takes the maximum within all calculation times.

(iv) The focused beam is reflected by the defect to generate echoes, which are recorded by the elements as the received signals.

(v) The position of the focal point is constantly changed to scan the whole detecting area, during which the steps above are repeated.

2.3. Focusing in reception

When the focusing beams encounter the defect, they can be reflected to generate echoes, including the P- and S-waves, which are separated in the received signals due to the difference in velocities. As mentioned before, each wave carries a specific type of information. Therefore, to make full use of the P- and S-waves in the received signals for imaging, the multi-wave focusing reception method is proposed. Similar to the focusing emission process, the P- and S-waves in the received signals can also be coherently superposed in the post-processing by controlling the time delays. Specifically, the following steps are taken:

(i) One assumes that there is a defect occurring at the focal point, and the received signals of the j-th element are denoted as $s_j(t)$. Also, by taking the received signal of the 1st element as the reference signal, the received signal of other elements can be delayed and superposed on that to make all the reflected P-waves in the received signals focused. And this method also holds true for the focusing reception of the reflected S-waves. It is interesting to note that the propagation paths of received echoes are exactly consistent with that of the incident waves, which means that the time delays for focusing reception are the same as those for focusing emission. So, the independent focusing reception process of P- and S-waves can be achieved using the following formulas:

$$S_p(t) = \sum_{j=1}^{N} s_j(t-\delta_j),$$
$$S_s(t) = \sum_{j=1}^{N} s_j(t-\tau_j), \quad (10)$$

where $S_p(t)$ is the focusing received signals of the reflected P-waves, and $S_s(t)$ is the focusing received signals of the reflected S-waves. If there is no actual defect occurring at the focal point, all signals are incoherently superposed, which only results in very weak noise signals.

(ii) Again, the focusing received signals of P- and S-waves can be delayed and coherently superposed to form the

multi-wave focusing received signals, which can be achieved using the following formula:

$$S_{\mathrm{f}}(t) = S_{\mathrm{p}}(t-\delta_1) + S_{\mathrm{s}}(t-\tau_1). \tag{11}$$

Here, the focusing process in reception for a single focusing emission has been completed. And $S_{\mathrm{f}}(t)$ is employed to be the multi-wave imaging signals.

(iii) As the position of the focal point is constantly changed, the imaging signals of the corresponding path can be obtained by repeating the steps above. Finally, the scanning image can be acquired.

3. Multi-wave focusing characteristics

In this section, the optimal array design parameters for good multi-wave focusing performance are given. And the influence of steering angles on the focusing energy is also studied, which indicates the available sweeping range of the multi-wave focusing method. Furthermore, the reflection characteristics of P- and S-waves are analyzed, which is helpful in understanding the advantages of the multi-wave focusing method in imaging.

In the numerical simulation, steel is chosen as the solid material, where c_{p} and c_{s} are about 5930 m/s and 3240 m/s. And to simulate the transient field in practical inspection, the cosine envelope function is employed to excite the elements, which is given as follows:

$$f(t) = \begin{cases} \frac{1}{2}\left\{1+\cos\left[\frac{2\pi}{t_{\mathrm{c}}}\left(t-\frac{t_{\mathrm{c}}}{2}\right)\right]\right\} \\ \times\cos\left[2\pi f_0\left(t-\frac{t_{\mathrm{c}}}{2}\right)\right], & 0 \le t \le t_{\mathrm{c}}, \\ 0, & t<0,\ \ t>t_{\mathrm{c}}, \end{cases} \tag{12}$$

where $f(t)$ is the time domain form of $F(\omega)$, f_0 is the center frequency and $t_{\mathrm{c}} = 2/f_0$. Here, the center frequency is chosen as $f_0 = 3.2$ MHz, in which case the wavelength of P-waves is $\lambda_{\mathrm{p}} = 1.8$ mm and the wavelength of S-waves is $\lambda_{\mathrm{s}} = 1$ mm.

3.1. Optimal array design parameters

Good beam focusing performance is the key to obtaining high-quality images, including the main lobe quality and side lobe amplitude, which can be observed in the radiation directivity pattern of the focusing field. Moreover, the focusing energy distribution along the steering angle is also an important aspect that should be considered.

For multi-wave focusing, the excitation energy of P-waves and S-waves should be balanced to make the most of two waves. If the focusing energy of any one wave is dominant, it makes that of the other one marginal. Typically, the relative intensity of excitation energy for two waves is determined by the element width. Here, the radiation energy of a single element with different sizes is shown in Fig. 2. It can be shown that the radiation energy of two waves can achieve a balance when the element width approaching $0.8\lambda_{\mathrm{s}}$ is employed. Besides, it also implies the different propagation characteristics of P- and S-waves, which is that the P-waves mainly propagate along lower steering angles, while S-waves propagate mainly along higher steering angles. These propagation characteristics provide them with different beam focusing and imaging characteristics.

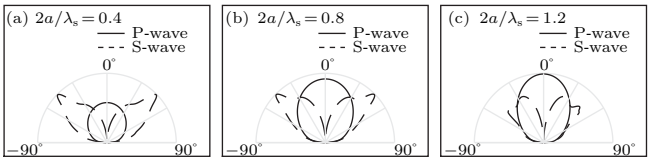


Fig. 2. The transient radiation energy patterns of the P- and S-waves radiated by a single element, which is excited by the cosine envelope.

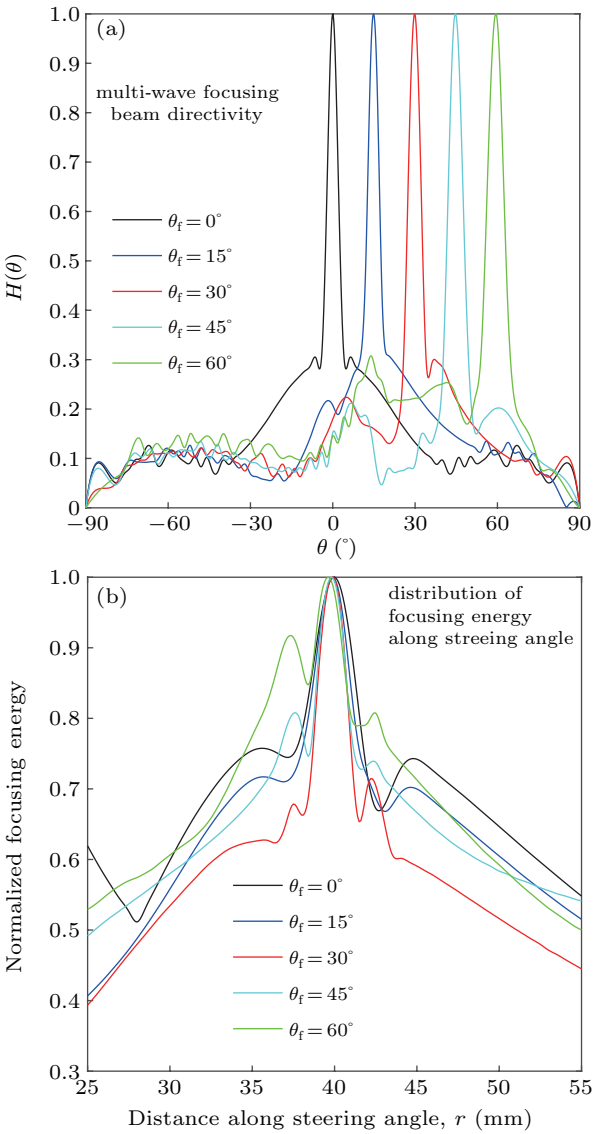


Fig. 3. The multi-wave focusing performance for various steering angles ($N = 16$, $2a/\lambda_{\mathrm{s}} = 0.8$, $d/\lambda_{\mathrm{s}} = 1.2$, $r_{\mathrm{f}} = 40$ mm).

To achieve the desirable beam focusing performance of S-waves, the inter-element spacing should not be larger

than $1.5\lambda_s$.[23] With regard to the improvements that larger inter-element spacing can provide for the focusing performance,[25,26] the inter-element spacing is chosen as $d/\lambda_s = 1.2$ in this paper.

As shown in Fig. 3(a), the high-quality main lobe is achieved, despite the slight increase in the main lobe width with the growth of the steering angle. And the side lobe amplitude is well suppressed, which implies the good focusing performance. One can observe in Fig. 3(b) that the position of the highest focusing energy coincides with the focal point, which also indicates a desirable beam focusing performance.

However, as shown in Fig. 4, the multi-wave focusing performance degrades significantly for $\theta_f > 65°$. The main lobe width and side lobe amplitude increase rapidly, which implies degradation of the focusing performance. Moreover, there is unstable fluctuation of the focusing energy around the predetermined focal point, which has deleterious influences on the inspection.

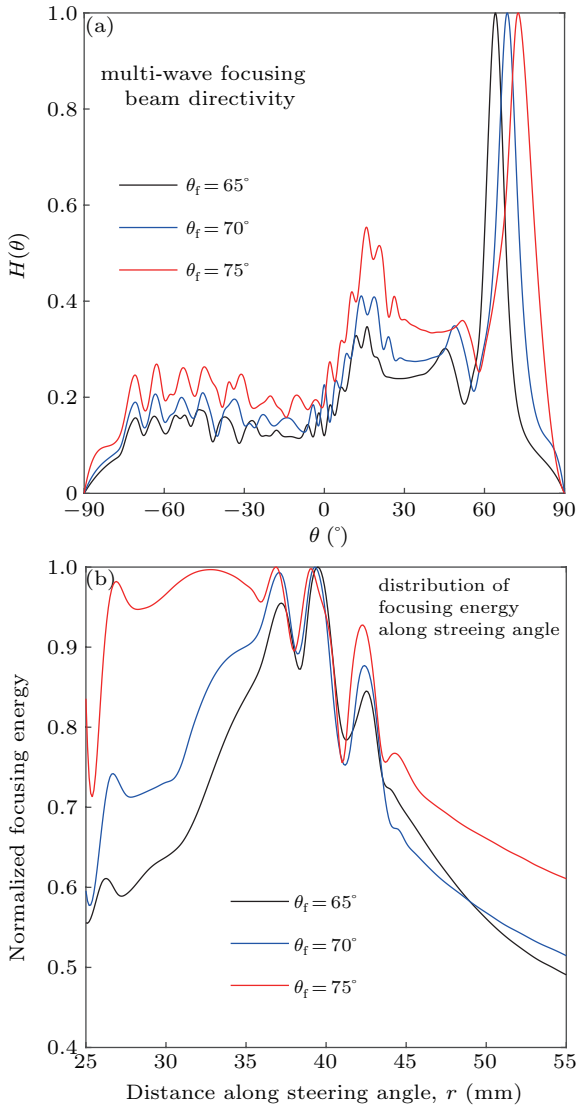


Fig. 4. The multi-wave focusing performance for higher steering angles ($N = 16$, $2a/\lambda_s = 0.8$, $d/\lambda_s = 1.2$, $r_f = 40$ mm).

3.2. Available sweeping range

In practical inspection, it is always desirable to enlarge the available sweeping range, in an attempt to reduce the mechanical movement of arrays and perform inspections for the medium with complicated structures. However, due to the propagation characteristics shown in Fig. 2, it is impossible to sweep through the entire half-space by employing the single wave focusing technology. In general, the P-waves are suitable for sweeping areas with lower steering angles, while S-waves are suitable for sweeping areas with higher steering angles.[22,23]

Figure 5 shows the variations in the focusing energy of three focusing methods for various steering angles. It can be observed that if -3 dB is taken as the criterion, the focusing energy of P-waves is concentrated in the steering angle range of 0°–35°, while that of S-waves is concentrated in the steering angle range of 30°–65°, respectively. Since multi-wave focusing technology combines the propagation characteristics of both P- and S-waves, it can achieve the desirable focusing energy in the steering angle range of 0°–65°, which expands the available sweeping range and improves the efficiency of inspection significantly. With regard to the symmetry, the available sweeping range is $-65°$ to 65°.

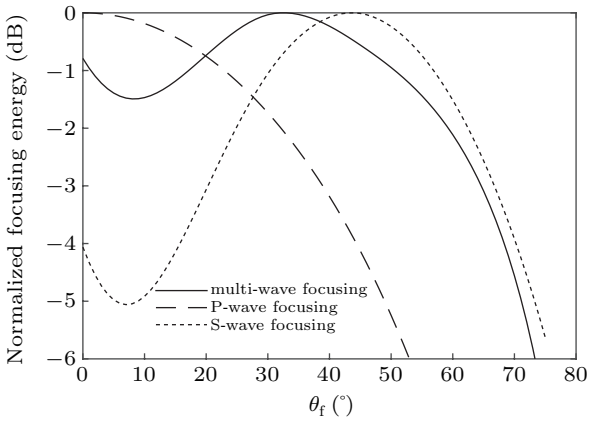


Fig. 5. The focusing energy of different focusing methods for various steering angles ($N = 16$, $2a/\lambda_s = 0.8$, $d/\lambda_s = 1.2$, $r_f = 40$ mm).

3.3. Reflection characteristics of P- and S-waves

Indeed, the focused beam can be regarded as the coherent superposition of the plane waves with various propagation directions. Similarly, the received signals can be regarded as the echoes of the focused beam reflected by the defect, which also originates from various directions. So, to understand the benefits of multi-wave focusing technology in imaging, it is important to analyze the reflection characteristics of P- and S-waves.

As shown in Fig. 6, the P- and S-waves are incident on the surface of the defect with the incident angle of γ_1. Each of them can generate P- and S-waves by reflection and mode conversion. And the reflection angles of mode conversion in two

cases are denoted as γ_2 and γ_3, respectively. For multi-wave focusing, all the reflected waves are collected to image, which makes the most of the information from echoes.

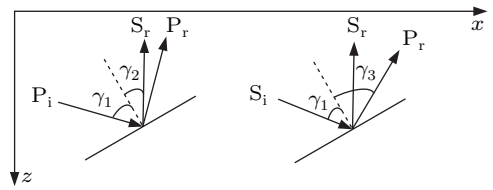


Fig. 6. A schematic of the reflection process for plane waves, where P_i and S_i are the incident waves, and P_r and S_r are the reflected waves.

The reflection of plane waves is a classical problem in wave motion and has been thoroughly studied. Assuming that the surface of the defect can be regarded as the free boundary, the reflection coefficients of various incident waves can be written as follows:[27]

$$\begin{aligned} R_{\rm pp}(\gamma_1) &= \left| \frac{\sin 2\gamma_1 \sin 2\gamma_2 - (D\cos 2\gamma_2)^2}{\sin 2\gamma_1 \sin 2\gamma_2 + (D\cos 2\gamma_2)^2} \right|, \\ R_{\rm ps}(\gamma_1) &= \left| \frac{2D\sin 2\gamma_1 \cos 2\gamma_2}{\sin 2\gamma_1 \sin 2\gamma_2 + (D\cos 2\gamma_2)^2} \right|, \\ R_{\rm ss}(\gamma_1) &= \left| \frac{\sin 2\gamma_1 \sin 2\gamma_3 - (D\cos 2\gamma_1)^2}{\sin 2\gamma_1 \sin 2\gamma_3 + (D\cos 2\gamma_1)^2} \right|, \\ R_{\rm sp}(\gamma_1) &= \left| \frac{D\sin 4\gamma_1}{\sin 2\gamma_1 \sin 2\gamma_3 + (D\cos 2\gamma_1)^2} \right|, \end{aligned} \tag{13}$$

where the first subscript denotes the type of incident wave, the second subscript denotes the type of reflected wave, $D = c_{\rm p}/c_{\rm s}$, and the reflection angles satisfy the conditions that $\sin(\gamma_2) = \sin(\gamma_1)/D$ and $\sin(\gamma_3) = D\sin(\gamma_1)$.

The variations in reflection coefficients for various incident angles are plotted in Fig. 7. It can be observed in Fig. 7(a) that the reflection coefficients of two waves tend to be complementary. For example, when $R_{\rm pp}$ tends to decrease, $R_{\rm ps}$ tends to increase, which compensates for the shortcomings of each other. On the other hand, in Fig. 7(b), the value of $R_{\rm ss}$ climbs sharply around the incident angle of 30°, which is caused by the total reflection of S-waves. This is a common phenomenon for S-waves and has been intensely studied,[10,27] and lies outside the scope of this paper and is thus not analyzed.

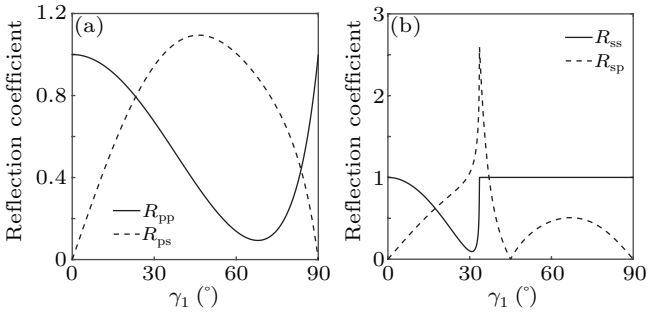


Fig. 7. The reflection coefficients for various incident angles: (a) the incident wave is a P-wave, (b) the incident wave is an S-wave.

In summary, the advantages of the multi-wave focusing method originate from the combination of the propagation and reflection characteristics for P- and S-waves, which can strengthen the reflected echoes originating from various propagation directions and sweeping areas. Thus, the multi-wave focusing method can improve the imaging distinguish ability of defects.

4. Experiment result

In this section, an imaging experiment is performed to verify the results of the theoretical analysis, which visually presents the outstanding advantages of the multi-wave focusing method. As shown in Fig. 8, a steel block with thirteen circular through-holes is selected as the test block. The array parameters in the experiment are the same as those in numerical simulation. And the Verasonics Vantage Research System is employed in this experiment, which is a programmable ultrasonic system and thus provides a flexible platform for researchers.

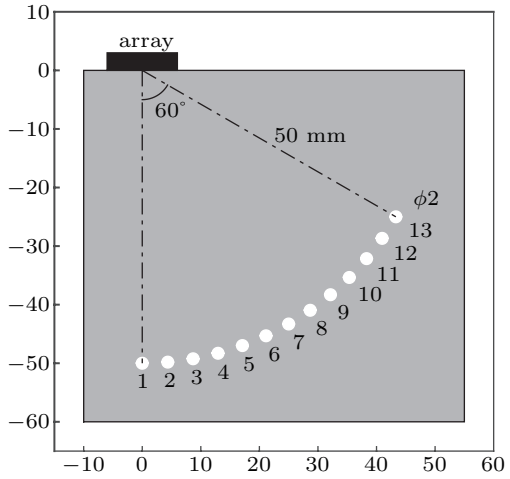


Fig. 8. The structure diagram of the test block, where thirteen circular through-holes with the diameter of 2 mm are evenly distributed on the arc line with the diameter of 50 mm and sequentially numbered as Nos. 1–13, and $\phi 2$ indicates that the diameter of a hole is 2 mm.

Here, the sector scanning images for the traditional single wave focusing method and multi-wave focusing method are given in Fig. 9, where the imaging area is within the steering angle of −10°–65°. There are no defects in the left half plane, so the image of that area is not given.

To quantitatively evaluate the distinguish ability of defects in the image, the imaging signal-to-noise ratio of the n-th defect can be defined as

$$\sigma(n) = 20\lg\frac{I(n)}{I_{\max}}, \tag{14}$$

where $I(n)$ is the pixel value of the center pixel point of the n-th defect in the image, $I_{\max}$ is the maximum pixel value in the whole image, and the unit of $\sigma(n)$ is dB. Obviously, a higher

value of $\sigma(n)$ indicates better distinguish ability of the n-th defect in the image. Instead, the $\sigma(n)$ less than -6 dB indicates that the n-th defect cannot be successfully distinguished in the image.

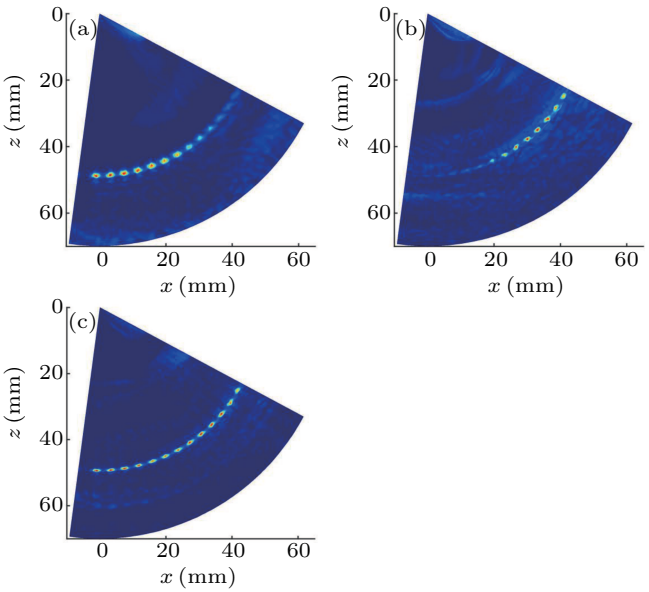


Fig. 9. The sector scanning images for (a) the single wave focusing method of P-waves, (b) the single wave focusing method of S-waves and (c) the multi-wave focusing and imaging method.

As shown in Fig. 9(a), the P-wave focusing method can only provide a desirable distinguish ability for the defects Nos. 1–6 that are located at lower steering angles, which is consistent with the propagation characteristics of the P-wave. With the increase in the steering angle, the distinguish ability of the defects gradually degrades. In contrast, it can be shown in Fig. 9(b) that the S-wave focusing method can only provide a desirable performance at the higher steering angles, which is also consistent with the propagation characteristics of the S-wave. So, it can be observed that only defects Nos. 8–13 can be clearly distinguished in the image.

Obviously, as shown in Fig. 9(c), the multi-wave focusing and imaging method can provide the desirable distinguish ability for all defects, which benefits from the combination of the characteristics of multiple waves. This is particularly observed for defect No. 7 that is distributed along the steering angle of 30°, which achieves a significant improvement of imaging distinguish ability in Fig. 9(c). To quantitatively evaluate the improvements in the multi wave focusing method for the imaging distinguish ability of defects, the imaging signal-to-noise ratio of defects Nos. 6–8 for the various focusing methods are calculated and given in Table 1, which represents the imaging distinguish ability of defects distributed within the steering angle from 25°–35°. It can be shown that the imaging distinguish ability of defects within this area is poor for the single wave focusing method but is significantly improved for the multi-wave focusing method. This is due to the fact that the multi-wave focusing method strengthens the beam focusing energy by focusing the P-waves and S-waves in emission, which is helpful in improving the signal-to-noise ratio of echoes. And the scanning area within the steering angle from 25°–35° is the shared radiation range of P-waves and S-waves, which demonstrates that the imaging distinguish ability of defects in this area can be improved most significantly.

Table 1. The imaging signal-to-noise ratio of different defects for various focusing methods.

Defect number	$\sigma(6)$ (dB)	$\sigma(7)$ (dB)	$\sigma(8)$ (dB)
Fig. 9(a)	2.52	4.18	< -6
Fig. 9(b)	< -6	5.35	1.5
Fig. 9(c)	-0.63	-0.22	-0.43

So, it can be proved that the multi-wave focusing method can expand the imaging range, which is helpful in improving the detection efficiency. And it can also increase the signal-to-noise of echoes, which provides a significant improvement in the imaging distinguish ability of defects, especially for the defects located within the steering angle from 25°–35°.

5. Conclusion and perspectives

In an attempt to overcome the inherent limits of traditional single wave imaging for NDT, the multi-wave focusing and imaging method for linear phased arrays is studied, which makes the waves focused in both the emission and reception processes. The double pulse method is proposed to realize the multi-wave focusing process, and the focusing reception process is proposed to form imaging signals with a high signal-to-noise ratio. The numerical result shows that the element width approaching $0.8\lambda_s$ can maintain a balance between the radiation energy of two waves, which can achieve a desirable multi-wave focusing performance. Due to the combination of different propagation and reflection characteristics of P- and S-waves, the multi-wave focusing and imaging technology can expand the available sweeping range to the steering angle of $-65°$ to 65°, which also significantly improves the distinguish ability of defects.

Arrays with optimal parameters are employed to perform the imaging experiment for a steel block with defects. It is shown that the multi-wave focusing and imaging method can improve the imaging distinguish ability of defects over the traditional method using a single wave, especially for the defects distributed within the steering angle approaching from 25°–35°.

The multi-wave focusing and imaging method is of great importance in that it can provide a more comprehensive real-time image for the defects. And this method can be further expanded to the application of guided waves in NDT. So, it is

the authors' belief that the multi-wave focusing and imaging method has a promising future in the field of NDT.

References

[1] Younis W A, Stergiopoulos S, Havelock D and Grodski J 2002 *J. Acoust. Soc. Am.* **111** 2117

[2] Choi Y, Lee H, Hong H and Ohm W S 2011 *J. Acoust. Soc. Am.* **130** 2720

[3] Xu N and Zhou Z G 2014 *NDT & E Int.* **63** 28

[4] Brizuela J, Camacho J, Cosarinsky G, Iriarte J M and Cruza J F 2019 *NDT & E Int.* **101** 1

[5] Wei B, Zhou T, Li H, Xing T and Li Y 2019 *J. Acoust. Soc. Am.* **145** 3177

[6] Bertilone D C, Killeen D S and Bao C 2007 *J. Acoust. Soc. Am.* **122** 2679

[7] Tan J S, Frizzell L A, Sanghvi N, Wu S J, Seip R and Kouzmanoff J T 2001 *J. Acoust. Soc. Am.* **109** 3055

[8] Masoy S E, Varslot T and Angelsen B 2005 *J. Acoust. Soc. Am.* **117** 450

[9] Matte G M, Neer P L M J V, Danilouchkine M G, Huijssen J, Verweij M D and Jong N 2011 *IEEE Trans. Ultrason. Ferroelect. Freq. Contr.* **58** 533

[10] Dai Y X, Yan S G and Zhang B X 2019 *Acoust. Phys.* **65** 235

[11] Fink M and Tanter M 2010 *Phys. Today* **63** 28

[12] Yang S, Yoon B and Kim Y 2009 *NDT & E Int.* **42** 128

[13] Ye J, Kim H J, Song S J, Kang S S, Kim K and Song M H 2011 *NDT & E Int.* **44** 290

[14] Dupont-Marillia F, Jahazi M, Lafreniere S and Belanger P 2019 *NDT & E Int.* **103** 119

[15] Ye S G, Wu J R and Peach J 2000 *Ultrasound Med. Biol.* **26** 833

[16] Sandrin L, Tanter M, Catheline S and Fink M 2002 *IEEE Trans. Ultrason. Ferroelect. Freq. Contr.* **49** 426

[17] Gennisson J L, Provost J, Deffieux T, Papadacci C, Imbault M, Pernot M and Tanter M 2015 *IEEE Trans. Ultrason. Ferroelect. Freq. Contr.* **62** 1059

[18] Emelianov S Y, Li P C and O'Donnell M 2009 *Phys. Today* **62** 34

[19] Zhang J, Drinkwater B W, Wilcox P D and Hunter A J 2010 *NDT & E Int.* **43** 123

[20] Drinkwater B W and Wilcox P D 2006 *NDT & E Int.* **39** 525

[21] Sy K, Bredif P, Iakovleva E, Roy O and Lesselier D 2018 *J. Phys.: Conf. Ser.* **1017** 012005

[22] Zhang B X, Liu D D, Shi F F and Dong H F 2013 *Chin. Phys. B* **22** 014302

[23] Dai Y X, Yan S G and Zhang B X 2020 *Chin. Phys. B* **29** 034304

[24] Lhémery A, Calmon P, Lecœur-Taïbi I, Raillon R and Paradis L 2000 *NDT & E Int.* **33** 499

[25] Wooh S C and Shi Y 1999 *Wave Motion* **29** 245

[26] Azar L, Shi Y and Wooh S C 2000 *NDT & E Int.* **33** 189

[27] Brekhovskikh L M 1980 *Waves in Layered Media* (New York: Academic Press)